JOURNAL OF MATERIALS SCIENCE 30 (1995) 6075–6082

A study of the failure mechanisms in Al/Al_2O_3 and Al/SiC composites through quantitative microscopy

P. POZA, J. LLORCA
Department of Materials Science, Polytechnic University of Madrid, E. T. S. de Ingenieros de Caminos, 28040 Madrid, Spain

The failure mechanisms in tension and fatigue of three Al alloys reinforced with ceramic particulates were studied by means of optical and scanning electron microscopy. Damage was concentrated in the reinforcements, which failed in a brittle fashion during deformation, leading to the specimen fracture when a critical fraction of broken particulates was reached in a given section of the specimen. This critical fraction was measured on polished longitudinal sections of broken specimens for each composite, temper, and loading condition, and was mainly dependent on the matrix alloy. It was also found that the reinforcement fracture probability was controlled by the particulate size and aspect ratio: large and elongated particulates oriented in the loading direction were more prone to fail than small, equiaxed ones. Finally, a significant fraction of the reinforcements in the cast materials was broken prior to testing. They were shattered during extrusion rather than fractured, and associated with clusters of particulates formed during solidification.

1. Introduction

Specimens of very high purity of fcc and bcc polycrystalline metals strained in uniaxial tension usually fail by virtually a 100% reduction in area of the external neck which develops when the specimen becomes plastically unstable. However, engineering alloys always contain inclusions and second-phase particles, either added to improve the mechanical behaviour or not eliminated during processing and remaining as impurities. Their presence activates a different fracture mechanism, the material failing by the nucleation, growth and coalescence of voids [1], and the overall tensile ductility is reduced. The particles act as void nucleation sites during deformation by particle fracture or by interfacial decohesion, and these voids subsequently grow by plastic straining. Final fracture occurs suddenly by localized necking of the intervoid matrix.

The failure by nucleation, growth and coalescence of voids is a complex phenomenon, and the influence of the volume fraction, size and nature of the void nucleating particles on the fracture processes has been studied for many engineering alloys. In particular, Tanaka *et al.* [2], Broek [3], and Van Stone *et al.* [4] used quantitative microscopy and microprobe analysis to determine the void initiation sites in several high strength Al alloys strained in tension. Voids were nucleated in all cases at very low strains (around 2%) by fracture of large inclusions with an average size in the range 3 to 5 μm. The fraction of cracked particles increased with applied strain, and reached between 30 and 50% prior to the specimen fracture. The fraction of void nucleating inclusions present in the alloys was around 1 or 2%, and were identified by microprobe analysis as either Si- or Fe- and Mn-containing intermetallics. The particles with Fe and Mn cracked first, and those containing Si failed at higher strains. One of the Al–Cu alloys tested also presented void initiation by fracture of large $CuAl_2$ inclusions. The voids nucleated by inclusion fracture grew slowly during deformation, and the final coalescence took place by a combined mechanism of void impingement between closely spaced voids, or by the formation of void sheets between the more widely separated voids. Void sheets were composed of smaller voids nucleated by interfacial decohesion between the matrix and submicron-sized dispersoids.

It is generally accepted in metallurgy that ductility could be improved by decreasing the volume fraction of large inclusions which are broken earlier during deformation. However, the need for materials with higher stiffness and strength has led to the development of metal/ceramic composites, where a ductile matrix is reinforced with large volume fractions (typically 10 to 20%) of ceramic particulates. High strength Al alloys reinforced with either Al_2O_3 or SiC particulates are among the most promising composite material systems [5]. Evidently, the main drawback of these composite materials is their very low ductility, which is limited by the nucleation of voids by reinforcement cracking, as reported in the literature [6–10]. The assessment of factors influencing reinforcement fracture is thus critical, and it is particularly important to find out the effects of reinforcement size, aspect ratio and spatial distribution on particulate cracking. To this end, quantitative microscopy was used to determine the fraction and geometric characteristics of broken and intact reinforcements prior to

0022–2461

TABLE I Chemical composition (wt%) of the matrices

	Si	Cu	Mg	Mn	Fe	Cr	Zn	Ti	Ni	Al
2618 Al	0.18	2.30	1.60	–	1.10	–	–	0.07	1.00	Rem.
2014 Al	0.76	4.70	0.47	0.78	0.06	0.01	0.06	0.03	–	Rem.
6061 Al	0.62	0.24	0.94	0.04	0.07	0.10	0.02	0.01	–	Rem.

TABLE II Heat treatment temperatures and times

Material	Solution temperature (°C)	Solution time (h)	Ageing temperature (°C)	Ageing time (h)
Al 2618 + SiC	530	1	190	10
Al 2014 + Al_2O_3	502	2	160	16
Al 6061 + Al_2O_3	560	2	160	16

and after deformation in several Al-based composites reinforced with ceramic particulates.

2. Materials

Three different composite materials were used in this investigation: a 2618 Al alloy reinforced with SiC particulates, a 2014 Al alloy reinforced with Al_2O_3 particulates, and a 6061 Al alloy also reinforced with Al_2O_3 particulates. The first material was supplied by Cospray (UK) in the form of extruded rectangular bars (cross-section 25.4 mm × 62.5 mm), manufactured by spray co-deposition of the matrix and the SiC particulates. The other two composites were cast materials, supplied by Duralcan (USA) as extruded bars 50 mm in diameter. The chemical composition of the matrices (as provided by the manufacturers) is given in Table I. The volume fraction of ceramic reinforcements was nominally 15% in all cases.

The bars were received in the peak-aged (PA) condition, which involved a solution heat treatment, water quenching, and artificial ageing at elevated temperature. The temperatures and times used for each material are given in Table II. In the case of the 2618 Al-based composite, the bars were cold-stretched up to 2% after quenching to relieve the residual stresses. In addition, several specimens machined from the bars were solution heat treated again, to erase the effect of the prior thermal treatments, quenched in water, and naturally aged (NA) at room temperature during more than 4 days before testing.

3. Experimental techniques

3.1. Mechanical testing

Round specimens for the tensile and cyclic deformation tests were machined from the bars in the extrusion direction. The tensile specimens were 7.5 mm in diameter and 70 mm gauge length, while those tested in cyclic deformation were 12.5 mm in diameter and 25 mm gauge length to avoid buckling during compression. Both types of specimens were threaded to the load train. Two hinges, below and above the threaded connection, were used during the tensile tests to avoid bending stresses, and a precision alignment was given to the load train to minimize bending during the cyclic deformation tests. All the tests were finished at the specimen fracture.

The tensile tests were carried out in accordance with ASTM Standard E8M in stroke control under quasi-static conditions. Strains were recorded through a dynamic extensometer of 50 mm gauge length. The cyclic deformation tests were performed using the incremental step method which provides the complete cyclic stress–strain curve with one single specimen. Fully-reversed strain-controlled fatigue tests were carried out typically with an initial cyclic strain semi-amplitude of 0.3%. Load and strain (measured with a dynamic extensometer of 12.5 mm gauge length) were monitored in real time through a computer-controlled data acquisition system, and displayed on the computer screen. When the hysteresis stress–strain loop was stabilized (usually after a few tenths of cycles, although the number of cycles required to reach the steady-state condition was always higher in the naturally aged materials), the cyclic strain semi-amplitude was increased by 0.1%. This procedure was repeated until complete failure of the specimen. A cyclic frequency of 0.2 Hz (sinusoidal wave form) was employed in all the fatigue tests.

3.2. Specimen preparation

Metallographic samples of all the materials were prepared in the longitudinal (extrusion) direction before and after testing. The specimens were cut through the middle with a low-speed diamond blade wheel to minimize damage, using oil as a lubricant, and initially polished on SiC abrasive paper to 600 grit finish. This was followed by polishing on diamond slurry (9, 3 and 1 μm) and finally on magnesia. The polished samples were first cleaned in deionized water, and afterwards by ultrasound in acetone, and were observed by means of optical and scanning electron microscopy, using secondary- and back-scattered electrons, as well as energy-dispersive X-ray microanalysis.

3.3. Quantitative microscopy

In order to quantify the failure micromechanisms, micrographs were systematically taken from the longitudinal surfaces of the broken specimens at different distances from the fracture surfaces (0, 1, 2, 3, 4 mm, and further away). The micrographs for the quantitative analysis were taken using secondary electrons in the scanning electron microscope at a constant magnification of 1000. Optical micrographs were only used at the beginning of the investigation for the broken tensile specimens of the 2618 Al-based composite, and

TABLE III Number of ceramic reinforcements analysed for each material, temper and loading condition

Material	Monotonic, NA	Cyclic, NA	Monotonic, PA	Cyclic, PA
Al 2618 + SiC	1111	908	1016	816
Al 2014 + Al_2O_3	422	967	468	915
Al 6061 + Al_2O_3	462	812	–	859

TABLE IV Geometric characteristics of the ceramic particulates in the longitudinal direction

Material	$\bar{A}$ (μm^2)	$\bar{D}_{max} \pm SD$ (μm)	$\bar{D}_{min} \pm SD$ (μm)	Aspect ratio $\pm$ SD D_{min}/D_{max}
Al 2618 + SiC	57.7	12.2 ± 6.8	5.6 ± 2.5	0.46 ± 0.18
Al 2014 + Al_2O_3	140	21.3 ± 6.9	8.3 ± 3.4	0.41 ± 0.17
Al 6061 + Al_2O_3	144	19.3 ± 5.7	9.6 ± 3.2	0.51 ± 0.19

the magnification was slightly lower (× 600). The composite micrographs were digitized by means of a high-resolution scanner, and passed to a computer-controlled image analysis system. The particulate contours were obtained either automatically (by using the appropriate filters when the contrast between the matrix and the ceramic reinforcements was good enough) or manually, and the geometric characteristics of each particulate were calculated by the image analysis program. The main parameters obtained for each particulate were the area (A), the maximum (D_{max}) and minimum (D_{min}) dimensions, and the aspect ratio (D_{min}/D_{max}). The area was obtained from the number of pixels enclosed within the particulate contour. The maximum and minimum dimensions were those of an ellipse which had the same centroid and second moments of area as the particulate.

The study was carried out separately for intact and broken reinforcements, and the total number of particulates analysed for each material, temper and loading condition is given in Table III. In addition, the polished surfaces in the longitudinal direction were examined prior to testing, to obtain the fraction of reinforcements which were broken during processing.

4. Results and discussion

4.1. Reinforcement geometric characteristics

The average values of the area ($\bar{A}$), maximum ($\bar{D}_{max}$) and minimum ($\bar{D}_{min}$) dimensions, and aspect ratio in the longitudinal (extrusion) direction are given in Table IV for each composite in the NA condition. The results in the PA condition were very similar, and are not reported here. The SiC particulates were on average smaller than the Al_2O_3 reinforcements, although the size distributions were very wide for both. The SiC particulate size (understood as the square root of the area) was in the range 3 to 20 μm, with an average value of 7.5 μm, whereas the Al_2O_3 reinforcements exhibited an average size of 12 μm, with particulates between 5 and 22 μm.

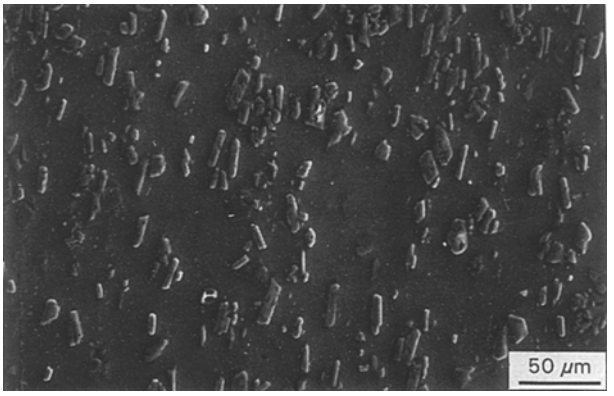

Figure 1 Low magnification micrograph of the 2014 Al-based composite. Notice that the Al_2O_3 particulates are oriented with their longer axes in the extrusion direction.

The aspect ratio distributions were similar for all the reinforcements, with average values in the range 0.41 to 0.51 and standard deviations around 0.18, which again are indicative of a wide distribution. In fact, equiaxed (aspect ratio $\geqslant 0.9$) and very elongated (aspect ratio $\leqslant 0.2$) particulates were found in the three materials. It is worth noting that the reinforcements were oriented with their longer dimension parallel to the extrusion axis (Fig. 1).

4.2. Reinforcement fracture during processing

Particulate–matrix decohesion was not observed during the detailed examination of the polished surfaces of the composites prior to testing. However, broken SiC and Al_2O_3 particulates were seen, although the fraction of broken reinforcements was significantly higher in the latter. Most of the broken Al_2O_3 particulates were found in regions where the ceramic particulates were very close together in a cluster, and they were shattered. This is shown for both materials in Fig. 2a and b. The Al_2O_3 particulates appear as dark grey zones, and were completely fractured or even reduced to small fragments in the case of the 6061 Al-based material. Porosity (black regions) was often associated with clusters of shattered particulates. In general, wherever clustered particulates were found, they were shattered, very likely during extrusion of the materials. This kind of failure was not observed in the SiC-reinforced composite, the difference being probably due to the rapid solidification of the spray formed material, which leads to a homogeneous distribution of the particulates in the matrix. On the contrary, the slower cooling rate of the cast composites tends to produce reinforcement segregation as a result of particulate pushing by an advancing solidification front. The ceramic reinforcements are concentrated in the interdendritic regions, leading to clusters of closely packed particulates. Subsequent extrusion contributes to better particulate distribution, but it may lead to localized reinforcement fracture in zones where the particulates are clustered.

Some isolated particulates not linked to a cluster were also broken but the fracture mode was

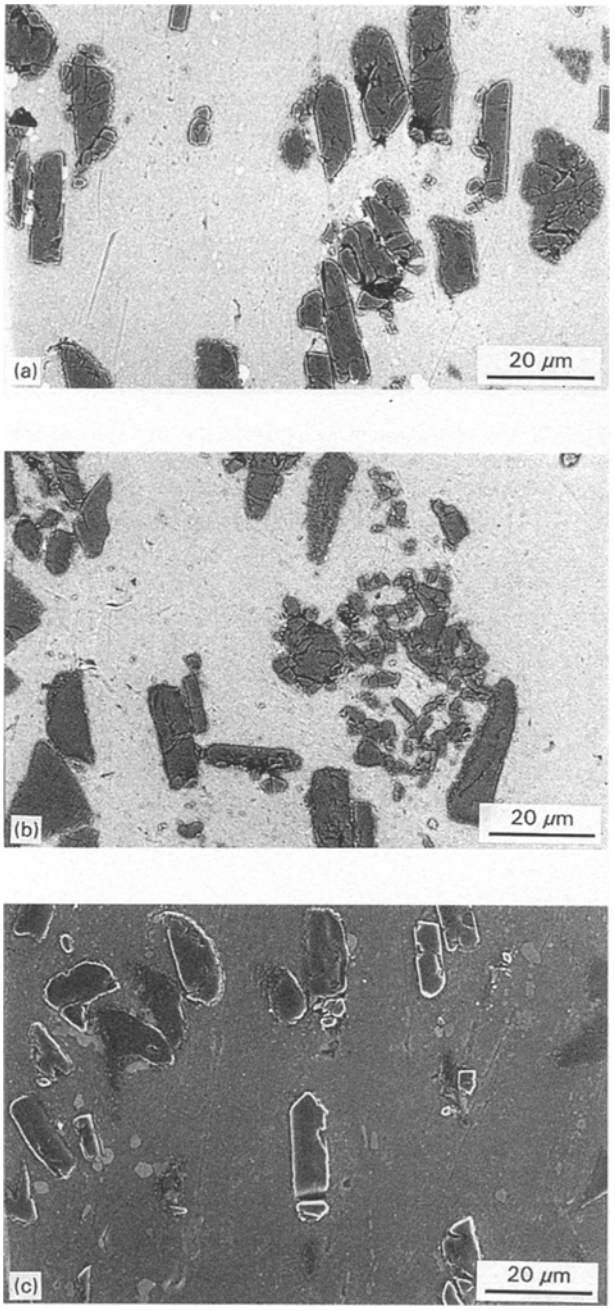

Figure 2 (a) Back-scattered electron micrograph of a cluster of shattered particulates in the 2014 Al alloy reinforced with 15 vol % Al_2O_3 particulates (PA). Al_2O_3 particulates are seen as dark grey zones, whereas intermetallic inclusions (made up of Al, Cu, and Mn) are white. (b) Back-scattered electron micrograph for the 6061 Al alloy reinforced with 15 vol % Al_2O_3 particulates (PA). (c) Secondary electron micrograph of the 2014 Al alloy reinforced with 15 vol % Al_2O_3 particulates (PA) showing an isolated broken particulate. All the micrographs were taken on the as-received materials prior to testing. Extrusion axis is vertical in all cases.

completely different in this case, with the reinforcement being fractured by a single crack perpendicular to the extrusion direction (Fig. 2c). The fracture of isolated particulates was, however, much less important than damage associated with clusters, as is indicated in Table V, where the percentage of isolated and clustered broken reinforcements is given for each composite. These results also show that the 6061 Al-based composite was more damaged prior to testing, presenting a significant fraction of shattered Al_2O_3 particulates in clusters. On the contrary, damage in

TABLE V Fraction of broken particulates in the as-received materials

Material	Isolated particulates (%)	Clustered particulates (%)
Al 2618 + SiC	2.0	–
Al 2014 + Al_2O_3	5.5	8.5
Al 6061 + Al_2O_3	2.7	13.0

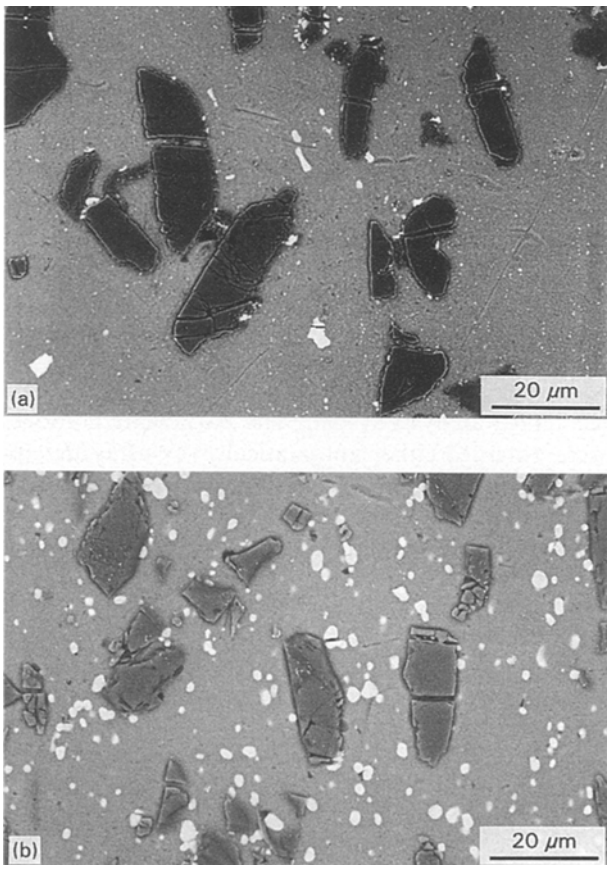

Figure 3 Back-scattered electron micrographs of the longitudinal sections of the composites tested in tension, where reinforcements broken by cracks perpendicular to the loading axis (vertical) are seen. (a) 2014 Al alloy reinforced with 15 vol % Al_2O_3 particulates in the peak-aged condition. (b) 2618 Al alloy reinforced with 15 vol % SiC particulates in the naturally aged condition. The white areas in both micrographs stand for intermetallic inclusions.

the composite reinforced with SiC was minimal, and only 2% of the particulates were fractured.

4.3. Failure micromechanisms

The analysis of the longitudinal sections of the composites after testing demonstrated that the initial damage mechanism during deformation was reinforcement fracture. Two back-scattered electron micrographs from specimens tested under monotonic tension are shown in Fig. 3, where Al_2O_3 and SiC reinforcements broken by cracks perpendicular to the loading axis are clearly seen. The white areas in both micrographs stand for the intermetallic inclusions present in the matrix. Energy-dispersive X-ray microanalysis indicated that they were made up of Al, Cu, and Mn in

the 2014 Al matrix and of Al, Ni and Fe in the 2618 Al matrix. These inclusions were the void nucleation sites in the unreinforced alloys [9] but not in the composites, where damage had accumulated in the ceramic particulates. Sometimes, one intermetallic inclusion was broken (see Fig. 3a), but this was unusual, and the fraction of broken inclusions was negligible when compared to the fraction of broken ceramic reinforcements.

In addition to the particulates broken by cracks perpendicular to the loading axis, shattered reinforcements in clusters were also observed in the Al_2O_3-reinforced composites. However, their morphology indicated that they were broken prior to deformation and not during the tests. In addition, Al_2O_3 particulates broken by cracks parallel to the loading axis were seen in the specimens strained under cyclic deformation. The same fracture morphology was found by Yang *et al.* [11] on an Al/SiC composite tested in monotonic compression, and it can be concluded that they were fractured during the compressive part of the loading cycle. The fraction of reinforcements broken in compression was, however, quite small (about 2% for the 2014-based composites and 4% for the 6061-based materials), and this mechanism of void initiation was not important from the point of view of damage.

The fraction of broken reinforcements as a function of the distance to the fracture surface is shown in Fig. 4a to c for the three materials and loading conditions. Only the particulates broken by one or several cracks perpendicular to the loading axis are included in these results. Despite the experimental scatter, it is worth noting that the fraction of broken reinforcements around the fracture surfaces was to some extent controlled by the matrix alloy and independent of the temper and loading conditions. This value was slightly over 20% for the 2618 Al-SiC composites and higher (between 30 and 50% if the particulates in clusters which were broken prior to deformation are included) for the other two materials. The main difference between the specimens tested in monotonic tension and cyclic deformation was damage localization. Reinforcement fracture was spread throughout the specimen length during the tensile tests, and concentrated around the fracture region in fatigue. In fact, the fraction of broken reinforcements above two millimetres below the fracture surface was almost constant for the specimens loaded in fatigue, and very close to the fraction of isolated reinforcements which were broken prior to deformation (Table V). For instance, around 6% of the particulates were found to be broken during cyclic deformation in the 2014 Al-based composites far away from the fracture surfaces, whereas 5.5% of isolated Al_2O_3 particulates were found broken prior to deformation in this composite. The analysis of the experimental results for the other two materials also led to the conclusion that damage during fatigue was concentrated around the fracture region.

Decohesion at the particulate/matrix interface was not observed, indicating that the bonding between matrix and reinforcements was very good. The

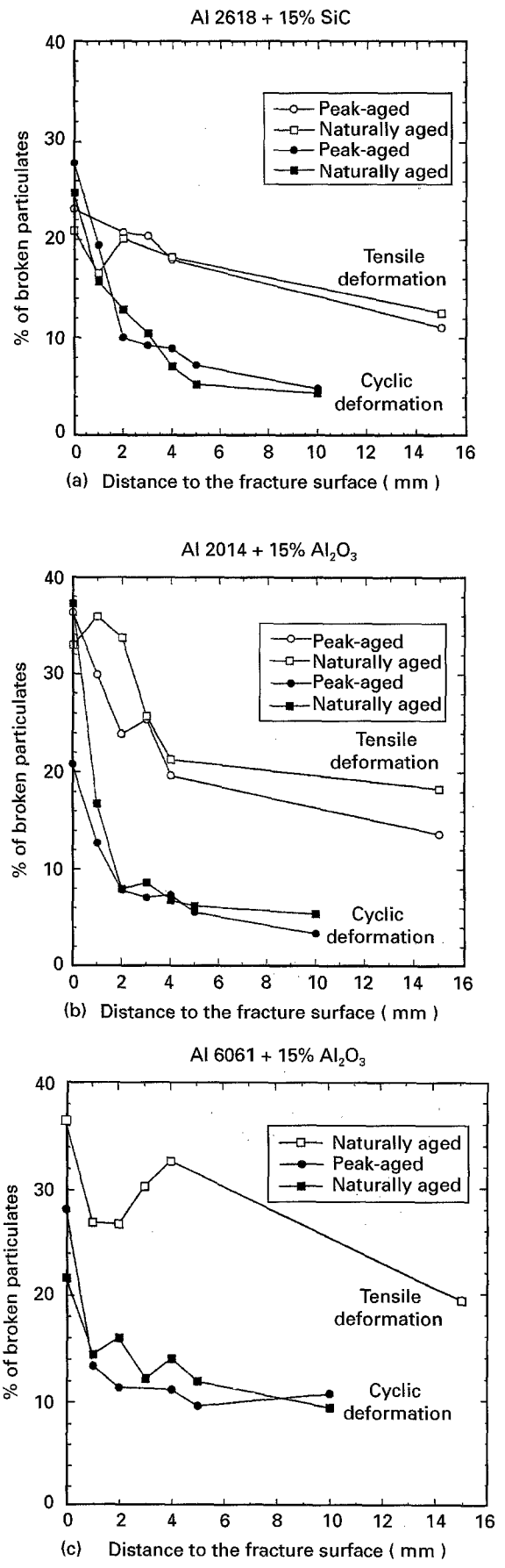

Figure 4 Fraction of broken particulates by one or more cracks perpendicular to the loading axis during monotonic (open symbols) and cyclic (solid symbols) deformation as a function of the distance to the fracture surface. (a) Al 2618 reinforced with 15 vol % SiC particulates. (b) Al 2014 reinforced with 15 vol % Al_2O_3 particulates. (c) Al 6061 reinforced with 15 vol % Al_2O_3 particulates. Particulates shattered in clusters, broken prior to deformation, and those broken during cyclic deformation by cracks parallel to the loading axis were not included.

displacement continuity at the interface allowed a load transfer from the matrix to the reinforcement during deformation as a consequence of the differences in the elastic constants between the Al matrix and the ceramic particulates. In addition, the matrix starts to flow plastically as deformation progresses, and high triaxial stresses are developed within the composite due to constraints imposed on the matrix plastic flow by the hard ceramic reinforcements [12, 13]. This process enhances the apparent matrix flow stress during plastic deformation, and consequently the amount of load transferred to the reinforcements. Once the stresses acting on the particulate reached the reinforcement strength, the particulate was fractured by a crack perpendicular to the direction of the maximum principal stress. Elongated particulates which were oriented in the loading direction were sometimes broken by two parallel cracks because the reinforcement was re-loaded again through the end and lateral surface of the particulates after the first crack appeared.

Once a particulate was broken, the process of void growth started. Void growth took place along the loading axis, as can be seen just below the fracture surface (Fig. 5a and b). Void growth in the direction perpendicular to the loading axis was inhibited by the strong bond between the matrix and the reinforcement. In addition, void growth was seen in some particulates just below the fracture surfaces and not far away (see Fig. 3a and b). It is difficult to estimate with accuracy the contribution of the void growth mechanism to the overall composite ductility, but it seems very likely that it is not important for these materials when tested in tension or fatigue. Void growth is a key process to assess the ductility in materials with low volume fractions of particles, where extensive enlargement of the voids is needed to reach the critical condition for coalescence. These materials fail at very large strains, developing localized necking, and the presence of large deformations and of high positive hydrostatic stresses at the centre of the necked region are necessary conditions for significant void growth [14]. On the contrary, particulate-reinforced metal–matrix composites exhibit low ductilities (usually a few per cent), and necking around the fracture region was not observed. It could be argued that positive hydrostatic stresses were already present at local level in the composite due to the constraint imposed by the ceramic reinforcements on the matrix flow. However, these hydrostatic stresses are relieved by particulate fracture, and the triaxiality levels around broken reinforcements are far lower. These facts, together with the large fraction of broken reinforcements found around the fracture surfaces, show that specimen failure took place when a critical fraction of broken reinforcements was reached in a given section, the contribution of void growth being of second order. Thus it is important to find the influence of the reinforcement geometric characteristics on the particulate fracture probability in order to improve the overall ductility of metal–matrix composites.

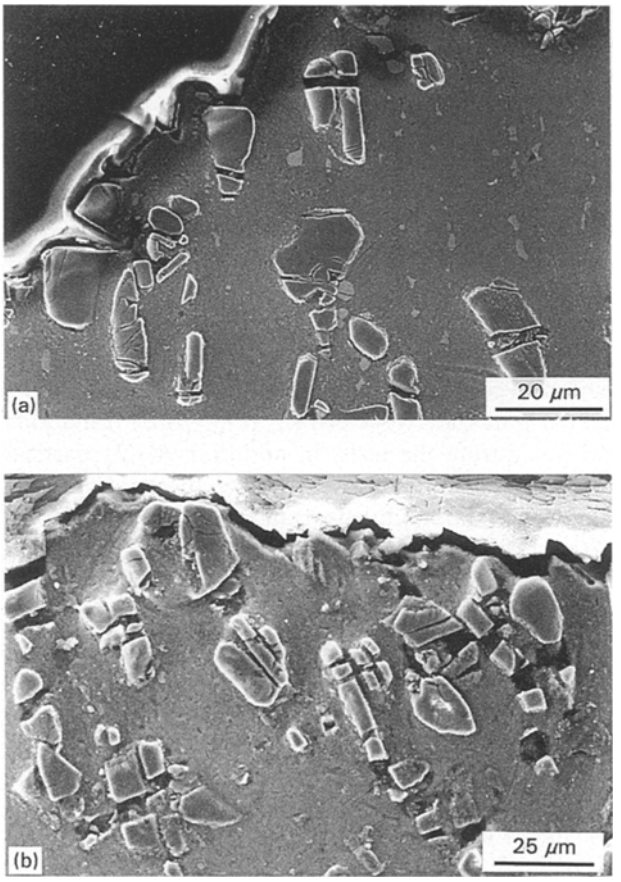

Figure 5 Formation of voids from broken ceramic particulates just below the fracture surface. (a) 2014 Al alloy reinforced with Al_2O_3 particulates (NA). (b) 6061 Al alloy reinforced with Al_2O_3 particulates (NA). Loading axis was vertical.

4.4. Influence of reinforcement size

A statistical analysis of the size of broken and intact reinforcements was carried out on the specimens tested in tension. Only the particulates broken by one or more cracks perpendicular to the loading axis were studied. The results are shown in Fig. 6a and b, where the cumulative fracture probability, F_d, is plotted as a function of the reinforcement size, D, which stands for the square root of the particulate area. For a given reinforcement size, $F_d(D)$ was obtained as the quotient between the number of broken particulates whose size was $\leqslant D$ and the total number of particulates (including intact and broken) whose size was $\leqslant D$. So $F_d(D)$ expresses the fracture probability for reinforcements with a size $\leqslant D$, and $F_d(D_{max})$ stands for the average fraction of particulates broken during tensile deformation in each material. It should be noted that $F_d(D)$ depends on the actual particulate size distribution within the composite (which was different for SiC and Al_2O_3), so the results in Fig. 6a and b cannot be compared directly. In addition, the fraction of broken reinforcements decreased with the distance from the fracture surface, and the cumulative fracture probabilities are also influenced by the proportion of reinforcements sampled at different distances from the fracture surface.

Despite the previous remarks, the results in Fig. 6a and b clearly demonstrate that the fracture probability

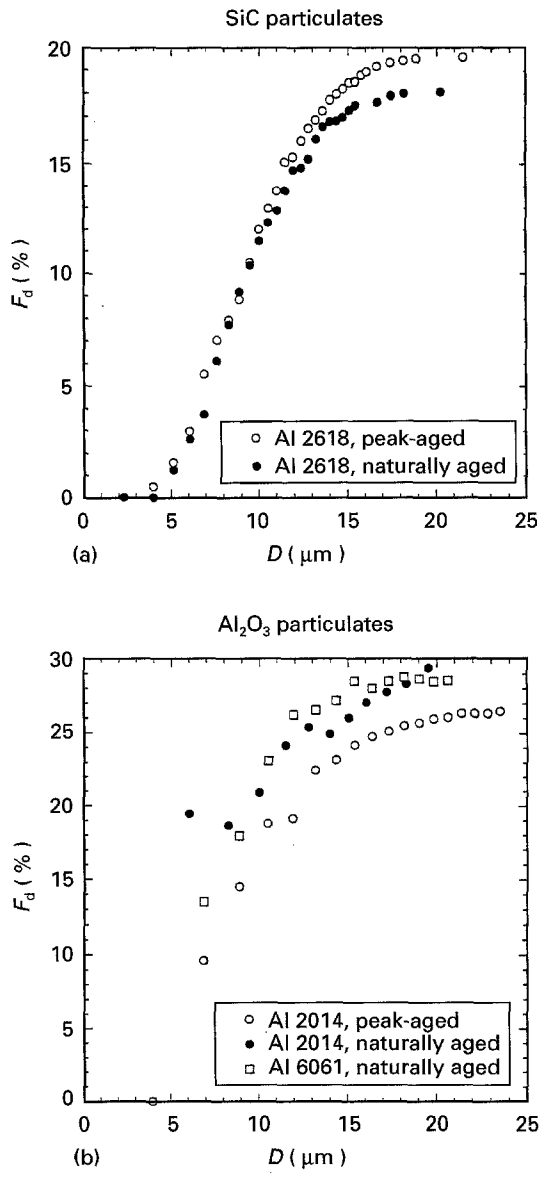

Figure 6 Cumulative fracture probability, F_d, as a function of the reinforcement size, D. (a) SiC particulates. (b) Al_2O_3 particulates. Only reinforcements fractured by cracks perpendicular to the loading axis were included.

increases with the reinforcement size. SiC and Al_2O_3 reinforcements below 5 μm were never broken. On the contrary, SiC particulates over 17 μm were always fractured. The quantitative results for Al_2O_3 were similar, although the experimental scatter was higher due to the smaller number of particulates sampled (see Table III).

The higher fracture probability of large particulates can be a consequence of either an increase in the stresses acting on the reinforcement or a decrease in the reinforcement strength. For the reinforcement sizes usually found in metal–matrix composites, continuum–plasticity models are applicable to describe the load transfer from the matrix, and they are insensitive to the particulate size [14]. On the other hand, the brittle nature of reinforcement fracture (Fig. 3) indicates that it was triggered by the presence of a pre-existing defect of length a, which grew unstably in the plane perpendicular to the maximum principal stress once the critical condition for propagation was reached. According to the Griffith criterion for crack instability, the particulate strength σ_u and size D should be related by the expression,

$$\sigma_u D^{1/2} = \text{constant} \quad (1)$$

if all the defects had the same orientation and a/D ratio, and all the particulates were of the same shape. The inverse relationship between reinforcement size and strength is consistent with quantitative measurements on cracked iron carbides in steels [15] and copper oxide particles in copper matrices [16], as well as with our experimental results. In addition, the qualitative observations on inclusion cracking in high strength Al alloys reported in the introduction [2–4] also concluded that large inclusions failed earlier during deformation. However, the exact form of the relationship between σ_u and D is difficult to obtain because it requires accurate descriptions of particulate stresses within the composite, and also of the particulate strength. The former depend on geometric factors, such as particulate shape and spatial distribution, and on the matrix deformation properties, whereas the latter is controlled by the intrinsic fracture toughness of the particulates and by the size, orientation, and morphology of pre-existing defects. Different attempts were made in the past to analyse this problem, and the use of the weakest link statistics has proven to be the most successful approach so far [7, 9, 17]. However, it is clear that more research is needed to identify the critical factors controlling the fracture probability of ceramic reinforcements in metal–matrix composites.

4.5. Influence of reinforcement aspect ratio

The influence of reinforcement shape on the fracture probability was also analysed for the specimens tested in tension, and the results are given in Fig. 7a and b, where the cumulative fracture probabilities, F_{ar}, are given as a function of the aspect ratio. F_{ar} were calculated as F_d, and $F_{ar}(D_{min}/D_{max})$ stands for the fracture probability for reinforcements with an aspect ratio $\leqslant D_{min}/D_{max}$. The limitations of F_d are also applicable to F_{ar}, but the results show unmistakable evidence that the fraction of broken reinforcements increased as the aspect ratio decreased or, in other words, that elongated reinforcements were more likely to fail than equiaxed ones.

Aspect ratio effects can be qualitatively explained following the argument developed in the previous section, when it is taken into account that reinforcements were oriented with their longer axes in the loading direction. Even if the particulate size and aspect ratio are uncorrelated, elongated reinforcements oriented in the loading direction should exhibit a higher fracture probability because they carry more load and support higher stresses than equiaxed ones. More detailed quantitative models to predict the influence of reinforcement shape on the fracture probability are based on the weakest link statistics and are still under development [7, 9].

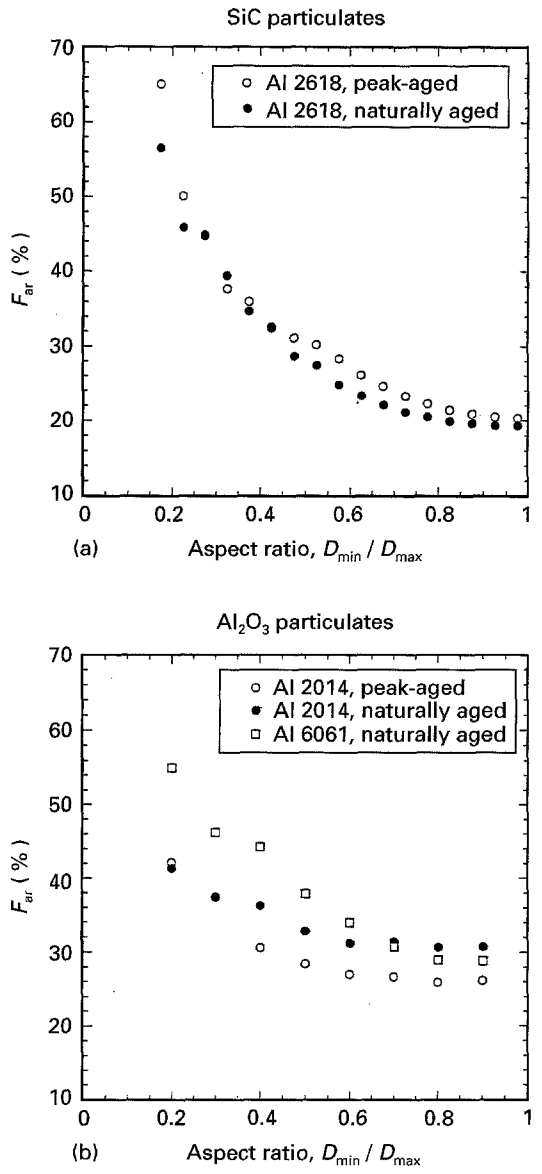

Figure 7 Cumulative fracture probability, F_{ar}, as a function of the reinforcement aspect ratio, D_{min}/D_{max}. (a) SiC particulates. (b) Al_2O_3 particulates. Only reinforcements fractured by cracks perpendicular to the loading axis were included.

5. Conclusions

The failure micromechanisms in particulate-reinforced metal–matrix composites under monotonic and cyclic deformation were analysed through quantitative microscopy. It was found that the dominant damage process was reinforcement fracture, regardless of the matrix composition, temper and loading mode. The reinforcements were broken during deformation by cracks perpendicular to the loading axis. Quantitative measurements indicated that failure took place when a critical fraction of broken particulates was reached in a given section of the specimen. In addition, it was found that the reinforcement fracture probability increased with its size, and that elongated particulates oriented in the loading direction were more likely to fail than equiaxed ones. Finally, a significant fraction of the reinforcements (about 15%) in the cast composites were found to be broken prior to testing. Broken reinforcements during processing usually presented a different fracture morphology, being shattered rather than fractured by a single crack, and were associated with clusters of particulates. These clusters of closely packed particulates were formed during solidification, and were most likely broken during extrusion.

Acknowledgements

This research was supported by the European Union through contract BREU-075C, and by CICYT, Spain, under grant MAT92-32.

References

1. R. H. VAN STONE, T. B. COX, J. R. LOW and J. A. PSIODA, *Inter. Metals Rev.* **30** (1985) 157.
2. J. P. TANAKA, C. A. PAMPILLO and J. R. LOW, in "Review of developments in plane strain fracture toughness testing", ASTM STP 463 (American Society for Testing and Materials, Philadelphia, 1970) p. 191.
3. D. BROEK, "A Study on Ductile Fracture", Report NRC-TR-71021U, Delft, National Aerospace Laboratory (1971).
4. R. H. VAN STONE, R. H. MERCHANT and J. R. LOW, in "Fatigue and fracture toughness: cryogenic behaviour", ASTM STP 556 (American Society for Testing and Materials, Philadelphia 1975) p. 93.
5. D. J. LLOYD, *Int. Mater. Rev.* **39** (1994) 1.
6. *Idem, Acta Metall. Mater.* **39** (1991) 59.
7. Y. BRECHET, J. D. EMBURY, S. TAO and L. LUO, *Acta Metall. Mater.* **39** (1991) 1781.
8. P. M. MUMMERY, B. DERBY and C. B. SCRUBY, *ibid.* **41** (1993) 1431.
9. J. LLORCA, A. MARTIN, J. RUIZ and M. ELICES, *Metall. Trans.* **24A** (1993) 1575.
10. P. M. SINGH and J. J. LEWANDOWSKI, *ibid.* **24A** (1993) 2531.
11. J. YANG, C. CADY, M. S. HU, F. ZOK, R. MEHRABIAN and A. G. EVANS, *Acta Metall. Mater.* **38** (1990) 2613.
12. T. CHRISTMAN, A. NEEDLEMAN and S. SURESH, *Acta Metall.* **37** (1989) 3029.
13. J. LLORCA, A. NEEDLEMAN and S. SURESH, *Acta Metall. Mater.* **39** (1991) 2317.
14. P. F. THOMASON, "Ductile fracture of metals" (Pergamon Press, Oxford, 1990).
15. T. LIN, A. G. EVANS and R. O. RITCHIE, *Metall. Trans.* **18A** (1987) 641.
16. K. WALLIN, T. SAARIO and K. TÖRRÖNEN, *Int. J. Fracture* **32** (1987) 201.
17. T. MOCHIDA, M. TAYA and D. J. LLOYD, *Mater. Trans. JIM* **32** (1991) 931.

Received 14 November 1994
and accepted 24 May 1995